Noninvasive Multi-parametric Imaging of Metastasis-Permissive Microenvironments in a Human Prostate Cancer Xenograft

Marie-France Penet[1], **Arvind P. Pathak**[1], **Venu Raman**[1], **Paloma Ballesteros**[2], **Dmitri Artemov**[1], and **Zaver M. Bhujwalla**[1],[*]

[1] JHU ICMIC Program, The Russell H. Morgan Department of Radiology and Radiological Science, The Johns Hopkins University School of Medicine, Baltimore, MD, 21205, USA

[2] Laboratory Organic Synthesis and Molecular Imaging by Magnetic Resonance, UNED, Madrid, Spain

Abstract

Metastasis continues to be one of the major causes of mortality from prostate cancer. Since human malignant cell lines metastasize more readily from orthotopic sites than from heterotopic sites, to identify metastasis-permissive tumor microenvironments, we used noninvasive imaging to compare the *in vivo* vascular, metabolic and physiological characteristics of a human prostate cancer xenograft implanted orthotopically in the prostate or subcutaneously in the flank. Hypoxia was detected in these xenografts by placing an enhanced green fluorescent protein (EGFP) optical reporter under the control of a hypoxia response element (HRE). A multi-parametric analysis of hypoxia, extracellular pH (pHe), vascularization and metabolism provided a characterization of environments that are permissive for metastasis to occur. We found that orthotopic tumors, which metastasized more easily, were characterized by higher vascular volume, permeability, and total choline, and a more acidic pHe. Interestingly, metastatic deposits in the lymph nodes as well as cancer cells in ascites fluid were found to be hypoxic, explaining in part, the refractory nature of metastatic disease. These results also provide the basis for clinically translatable noninvasive imaging markers for predicting metastatic risk in prostate cancer.

Keywords

prostate cancer; hypoxia; vascularization; choline metabolism; pHe; magnetic resonance spectroscopy and imaging; metastasis

Introduction

Prostate cancer is the most frequent cancer in men, and the second leading cause of death from cancer in men in the U.S (1). The vast majority of men dying of prostate cancer succumb to metastatic androgen refractory disease. Indeed, although localized prostate cancer can be treated with androgen ablation, surgical resection or radiation, its transition to metastatic disease is almost uniformly fatal (2).

Tumor microenvironmental parameters such as hypoxia, vascularization, choline metabolism, and extracellular pH (pHe) play key roles in cancer invasion and metastasis (3). The angiogenic phenotype is associated with aggressive and metastatic tumors that have increased

*Correspondence to: Zaver M. Bhujwalla, Ph.D., Department of Radiology, Johns Hopkins University School of Medicine, 208C Traylor Bldg, 720 Rutland Ave, Baltimore, MD 21205, Tel: (410)-955-9698, Fax: (410)-614-1948, zaver@mri.jhu.edu.

microvascular density (4). Tumor hypoxia results in the induction of genes associated with altered metabolism, angiogenesis and increased invasion and metastasis (5,6). Altered choline metabolism is one of the hallmarks of cancer, and increased total choline is associated with malignant transformation and an aggressive tumor phenotype (7). Extracellular acidosis has been associated with increased secretion of proteolytic enzymes as well as increased invasion and metastasis (8). In this study we sought to define the relationships between these microenvironmental parameters and metastasis *in vivo,* using noninvasive magnetic resonance imaging (MRI), magnetic resonance spectroscopic imaging (MRSI) and optical imaging.

Human malignant cell lines metastasize more readily from orthotopic sites than from heterotopic sites that are microenvironmentally unsuitable (9–11). To better understand the role of the tumor microenvironment in metastasis we compared the vasculature, total choline levels, hypoxia and pHe of a human prostate cancer xenograft model implanted subcutaneously, or orthotopically in the prostate. The use of PC-3 cells stably transfected to express enhanced green fluorescence protein (EGFP) under the control of a hypoxia response element (HRE), termed HRE-EGFP-PC-3 cells, allowed us to visualize hypoxia with optical imaging, while MRI and MRSI were used to characterize vascularization, total choline distributions and extracellular pH (pHe) in tumors derived from these cells. We used a microsurgical method of orthotopic implantation to avoid spilling and disseminating cancer cells during inoculation in the prostate. In this method, described by An *et al*. (12), intact tumor tissue is implanted in the prostate by suturing it into the lobes of the gland. By implanting tissues rather than injecting cells, the stromal tissue and the three dimensional cytoarchitecture, believed to play a critical role in tumor progression and metastasis, are initially maintained (12).

HRE-EGFP-PC-3 tumors in the orthotopic site of the prostate produced metastasis in the lymph nodes and liver, and similar to end-stage prostate cancer, the formation of malignant ascites that contained cancer cells. In contrast, implantation of similar-sized tissue from the same cells in the heterotopic site of the flank rarely resulted in metastasis. Hypoxia dependent EGFP expression of cancer cells in ascites fluid and lymph node metastases from orthotopic HRE-EGFP-PC-3 prostate cancer xenografts was observed suggesting that these environments were hypoxic. Since hypoxia is known to be a major cause of radiation and chemo-resistance and influences progression and aggressiveness (13–15), this may explain, in part, the refractory characteristics of metastatic prostate cancer.

Significantly higher vascular volume, total choline, lactate/lipid, and a more acidic pHe were detected in the orthotopic tumors. These studies have allowed us to identify non-invasive clinically translatable parameters that may assist in determining risk factors for formation of metastases in patients. These data also support exploring the use of anti-vascular or anti-angiogenic agents, targeting choline metabolism, and the modification of pHe as strategies for reducing metastasis.

Methods

Cell line and xenografts

Tumors were derived from PC-3 cells stably transfected with the HRE of human VEGF-A ligated to the EGFP gene (called HRE-EGFP-PC-3 cells). The expression of EGFP in these cells could be used to reliably detect hypoxia (16). PC-3 cells are androgen-independent human cancer cells, derived from a metastatic lesion of prostate adenocarcinoma in a lumbar vertebra. Solid tumors were derived from HRE-EGFP-PC-3 cells by inoculating 2×10^6 cells in 0.05 ml of Hanks Balanced Salt solution (Sigma, St. Louis) subcutaneously in the right flank of male severe combined immunodeficient (SCID) mice. Intact tumor tissue obtained from subcutaneous tumors was used for both orthotopic and subcutaneous implantation. For

orthotopic implantation, a piece of viable tumor tissue of approximately 1 mm^3 was implanted in the prostate of anesthetized SCID male mice by suturing it into the lobes of the gland under a surgical microscope. This was done to avoid the leakage and dissemination that might occur from inoculating a cell suspension in the gland. Sentinel mice were implanted subcutaneously with a similar sized piece of tumor tissue to provide a gauge of tumor growth, and for comparison with the orthotopic xenografts. Mice were scanned when tumor volumes were approximately 300 mm^3.

MR acquisitions

All imaging studies were done on a 4.7T Bruker Avance (Bruker, Billerica, MA) spectrometer using a home-built solenoid coil placed around the subcutaneous tumors, and a home-built volume coil placed around the lower torso of the mouse, for the orthotopic tumors. Mice were anesthetized with an intraperitoneal injection of ketamine (25 mg/kg; Phoenix Scientific, Inc., St Joseph, MO) and acepromazine (2.5 mg/kg; Aveco, Phoenix Scientific) diluted in saline. Multi-slice diffusion weighted images acquired with an in-plane spatial resolution of 250 μm × 250 μm (128 × 128 matrix, 32 mm field of view and a b-value of 100 mT/m) were acquired to localize the orthotopic tumors that appeared hyperintense in these images. The final diffusion-weighted images used to analyze the vascular and metabolic images were from the same 1 mm slices and 4 mm slice respectively.

Vascular imaging—The tail vein was catheterized before placing the animal in the spectrometer. Vascular imaging was performed as previously described (17). Briefly, multislice relaxation rate ($1/T_1$) maps were obtained by a saturation recovery method combined with fast T_1 SNAPSHOT-FLASH imaging (flip angle of 10°, echo time of 2 ms). First, an Mo map with a recovery delay of 7 s was acquired following which images of 4 slices (1 mm thick), acquired with an in-plane spatial resolution of 125 or 250 μm respectively (128 × 128 matrix, 16 mm field of view for the subcutaneous tumors and 32 mm for the orthotopic tumors, 8 averages), were obtained for three relaxation delays (100 ms, 500 ms, and 1 s). These T_1 recovery maps were obtained before i.v. administration of 0.2 ml of 60 mg/ml albumin-GdDTPA in saline (dose of 500 mg/kg) and repeated over a 21 minute period, starting 3 min after i.v. injection of albumin-Gd-DTPA. Albumin-GdDTPA was synthesized based on the method of Ogan *et al*. (18).

At the end of the imaging studies, the T_1 of blood was measured. Relaxation maps were reconstructed from data sets for three different relaxation times and the Mo dataset on a pixel-by-pixel basis.

Vascular volume and permeability-surface-area-product (PSP) maps were generated from the ratio of ($1/T_1$) values in the images to that of blood. The slope of ($1/T_1$) ratios versus time in each pixel was used to compute PSP, and the intercept of the line at zero time was used to compute vascular volume. Data were processed with an operator-independent computer program that enabled selection, mapping, and display of the regions with a routine written using Interactive Data Language (IDL, Research Systems, Boulder, CO). In addition to deriving the average of the detectable values of vascular volume and permeability over the entire tumor we analyzed regions of high vascular volume and high vascular permeability using a threshold for the highest 10% or 25% of the distribution (17,19).

Metabolic imaging—Metabolic maps of total choline (Cho) and lactate/lipid were obtained from a 4 mm thick slice using a 2D-chemical shift imaging (CSI) sequence with VAPOR water suppression (20). A reference image from a 4-mm-thick central tumor slice was acquired using a spin-echo sequence (msme-tomo, Bruker). Water-suppressed MRSI was performed on the same 4-mm-thick central slice, with an in-plane resolution of 1 mm × 1 mm per pixel using a

two-dimensional CSI sequence with VAPOR water suppression and the following variables: echo time (TE) of 272 ms, repetition time of 1089 ms, field of view (FOV) of 1.6 cm × 1.6 cm for the subcutaneous tumors and 3.2 cm × 3.2 cm for the orthotopic ones, 256 phase encode steps (16 × 16 voxels), number of scans (NS) of 8, block size of 1024, and sweep width of 4000 Hz. Reference two-dimensional CSI images of the unsuppressed water signal were acquired of the same slice with TE = 20 ms and NS = 2, with all other variables remaining the same. Quantitative maps in arbitrary units were generated according to the method described by Bolan *et al.* (21).

pHe imaging—*In vivo* imaging of pHe was performed as previously described by van Sluis *et al.* (22) using the chemical shift of the H-2 proton of the imidazolic pHe marker 2-imidazol-1-yl-3-ethoxycarbonyl propionic acid (IEPA). IEPA was injected intra-peritoneally (45 mg in 0.3 ml of saline neutralized to pH 7.0). pHe maps were obtained from a 4 mm thick slice using a 2D-CSI sequence with VAPOR water suppression using the following variables: TE of 23 ms, repetition time of 1,000 ms, FOV of 1.6 cm × 1.6 cm for the subcutaneous tumors and 3.2 cm × 3.2 cm for the orthotopic tumors, number of scans of 8, block size of 256, and sweep width of 10,000 Hz.

EGFP Expression—Optical images of EGFP expression were obtained from freshly cut tumor sections, as well as lymph nodes and ascites fluid. Cancer cells in ascites fluid were detected by bright field microscopy and examined for EGFP expression. It was possible to overlay the bright field microscopy images with the EGFP images and determine the presence or absence of EGFP in these cells.

For the lymph nodes EGFP expression was determined in excised fresh tissue containing the lymph nodes. Lymph nodes that fluoresced were fixed in formalin to confirm the presence of cancer cells with microscopy of hematoxylin and eosin (H&E) stained sections.

To quantify EGFP expression in the tumors, images from 2 mm thick slices were acquired on an inverted Nikon microscope, equipped with a filter set for 450–490 nm excitation and 500–550 nm emission and a Nikon Coolpix digital camera (Nikon Instruments, Inc.) and analyzed with ImageJ v1.34s (freeware for Windows developed by Wayne Rasband at the NIH).

Histological analyses of tumors and spontaneous metastasis

Tissues (tumor, liver, lymph nodes and lungs) were excised and fixed in 10% formalin for sectioning and staining. Lungs were inflated before fixation with a 0.5% agarose solution. Adjacent 5 μm thick histological sections were stained with H&E. Mitotic figures were counted in 20 fields of view of 7 different slides for both orthotopic and subcutaneous tumors. Tumor positive livers, lungs and lymph nodes were identified by optical microscopy examination of H&E-stained tissue sections. Lung and liver nodules were identified by microscopic examination of at least three 5 μm thick lung and liver sections per tumor bearing mouse.

Statistical analysis

Since we had no *a priori* knowledge of the shape of the underlying distributions for each of the assessed MRI and MRSI parameters, a two-tailed non-parametric Mann-Whitney U test was employed to determine if there was any significant (α=0.05) difference between these parameters for orthotopic versus heterotopic tumors. Consequently, data were plotted as box-and-whisker plots in which the length of each box is the interquartile range (IQR) and the line through the middle of each box is the median value of the parameter. The T-shaped lines extending from each end of the box represent the upper adjacent value (i.e. the largest observation ≤ 75th percentile+1.5×IQR) and the lower adjacent value (i.e. the smallest observation ≤ 25th percentile − 1.5×IQR), and gray dots denote parameter values outside this

range. In addition, to determine the feasibility of computing an *in vivo* "signature" of metastasis-permissive environments, we used a complete linkage hierarchical clustering technique on a dataset comprised of ten animals for which we acquired co-registered vascular volume, permeability-surface area product and total choline data, to determine if these three parameters were sufficient to stratify the data into two clusters corresponding to each microenvironment. To ensure that the different *in vivo* parameters were in comparable units, the data were scaled in Number Cruncher Statistical Systems (NCSS) using the standard deviation scaling method. All data were analyzed using NCSS (Kaysville, UT) for Windows.

Results

Higher vascular volume and higher permeability were observed in orthotopic tumors

Representative maps of subcutaneous (upper panel) and orthotopic (lower panel) tumors are shown in Figure 1A–C. In the orthotopic site, tumors were identified by the hyperintense signal detected in diffusion-weighted images (Figure 1A). The marked difference in vascular volume (Figure 1B) and PSP (Figure 1C) between the two implantation sites are evident in these representative maps. Differences in vascular volume and PSP between the two implantation sites (n=12 for orthotopic and 9 for heterotopic tumors) are summarized in Figure 1D. In addition to mean values of vascular volume and PSP of the entire tumor, analyses were also performed for the highest 10% and 25% values detected. As shown in these box-and-whisker plots, all three categories of vascular volumes were significantly higher in orthotopic tumors, while PSP was significantly higher in orthotopic tumors for the highest 10% and 25% values.

Metabolic maps of total choline and lactate/lipid revealed differences between orthotopic and subcutaneous tumors

Representative maps of subcutaneous (upper panel) and orthotopic tumors (lower panel) are shown in Figure 2A–B. As before, in the orthotopic site, tumors were identified by the hyperintense signal detected in diffusion-weighted images (corresponding diffusion-weighted images for these representative tumors are shown in Figure 1A). Total choline (Figure 2A) and lactate/lipid (Figure 2B) levels were significantly higher in the orthotopic (n=13) compared to the heterotopic (n=7) tumors. These differences are summarized in Figure 2C, and demonstrate the significantly higher total choline as well as lactate/lipid in the orthotopic tumors.

Complete linkage hierarchical clustering of ten animals for which co-registered vascular volume, permeability-surface area product and total choline data were acquired is shown in Figure 3. These three parameters were sufficient to stratify the data into two clusters corresponding to each microenvironment, demonstrating the feasibility of computing an *in vivo* "signature" of metastasis-permissive microenvironments for the PC-3 xenograft model.

Orthotopic tumors were more acidic than heterotopic tumors

Representative maps of subcutaneous (upper panel) and orthotopic (lower panel) tumors acquired to characterize pHe are shown in Figure 4A–B. Representative diffusion-weighted images, and the corresponding pHe maps obtained from the chemical shift of the pHe marker IEPA are shown in Figure 4A and B respectively. These data are summarized in Figure 4C, and demonstrate the significantly lower pHe in orthotopic tumors (n=10) compared to subcutaneous tumors (n=7).

Comparison of mitotic figures and hypoxia in primary tumors

Representative H&E stained sections demonstrating the difference in mitotic figures between a subcutaneous and an orthotopic tumor are shown in Figure 5A and B. Quantification of the mitotic figures in subcutaneous and orthotopic tumors are presented in Figure 5C and

demonstrate the significantly higher number of mitotic figures in the orthotopic compared to subcutaneous tumors.

Hypoxia, visualized by EGFP distribution within the tumor, was observed in both orthotopic and subcutaneous tumors (Figure 5D). Quantification of EGFP in orthotopic and subcutaneous tumor sections (n=5 for each group) did not reveal any significant difference either in the intensity of EGFP fluorescence or in the area (data not shown).

Characterization of metastasis

Lungs nodules were observed in 3/4 mice with subcutaneously implanted tumors and 3/3 mice with orthotopically implanted tumors. Only a few small clusters of cells were observed in the lungs of mice with subcutaneously implanted tumors (Figure 6A, left). In contrast, several large nodules were observed in mice with orthotopically implanted tumors (Figure 6A, right).

A representative H&E stained section obtained from the liver of a mouse implanted with an orthotopic tumor is shown in Figure 6B. Metastases were found in 60% of livers excised from orthotopically implanted mice (3/5 mice) but not in those excised from subcutaneously implanted mice (0/4 mice).

Hypoxic cancer cells were observed in the lymph nodes of mice with orthotopically implanted tumors (Figure 6C, left). We always observed cancer cells in fluorescing lymph nodes, but since we did not examine all the lymph nodes we cannot rule out the possibility that some non-fluorescing lymph nodes may have contained cancer cells. Mice with orthotopic tumors showed accumulation of ascites fluid that contained several fluorescing hypoxic cancer cells (Figure 6C, right). Subcutaneous tumors did not result in malignant ascites.

Discussion

Heterotopic and orthtotopic tumors derived from the same human prostate cancer cell line, displayed marked differences in metastasis, and significant differences in vascularization, total choline, lactate/lipids and pHe. Hypoxic cancer cells were observed in ascites fluid and lymph nodes. These results provide insights into metastasis-permissive environments, and demonstrate the importance of the tumor location in metastasis. In 1889, Stephen Paget observed that the pattern of metastatic dissemination was not random but that the cancer cell or 'seed' had an affinity for certain sites or 'soil' a phenomenon he termed 'the seed and soil effect' (23). Our results demonstrate that the 'soil' of the primary tumor also plays a critical role in metastatic dissemination.

Since the microenvironment of the tumor tissue that was implanted orthotopically or subcutaneously was similar to begin with, these data suggest that, depending upon the implantation site, cancer cells infiltrated differently following tumor growth.

In this study, we found that the same cell line presented with increased vascular volume and permeability from a metastasis-permissive orthotopic implantation site. A higher extent of preexisting blood vessels in the stroma of the murine prostate gland may have contributed to the increased vascularization in the prostatic microenvironment compared to the subcutaneous site (24).

While a direct comparison of the vasculature of orthotopic and heterotopic tumors from the same cell line is limited, some studies have been performed with different cancer models. Orthotopically implanted R3327 and MatLyLu prostate tumors displayed higher vascular permeability and vessel density compared to the subcutaneous tumors (25). Histological analysis of a human renal carcinoma showed that orthotopic implantation resulted in a higher

microvessel density (MVD) and more metastasis than subcutaneous implantation (26). A recent study, however, did not detect significant differences in vascular volume or permeability between subcutaneous and orthotopically implanted rat prostate tumor models but the occurrence of metastasis was not analyzed in the study (27).

Several pathological studies of histological specimens obtained from patients support the importance of MVD in metastatic dissemination (4). MVD characterization of histological specimens from prostate cancer patients demonstrated that increased MVD is predictive of metastasis (4). Similar correlations between MVD and metastasis have been observed in breast, pancreatic and esophageal cancer (28–30). Further support of the relationship between vascularization and metastasis is evident from observations that targeting angiogenesis and vascularization reduced metastasis in preclinical studies. Although the role of angiogenesis inhibitors in metastasis is becoming increasingly controversial (31), angiogenesis inhibitors have been effective in suppressing metastasis in preclinical cancer models of the lung (32), prostate (33,34) and brain (35). Aledronate, an aminobiphosphonate, was found to inhibit primary orthotopic PC-3 tumor growth and decrease the size of metastases, by inhibiting angiogenesis and increasing apoptosis (36).

We also observed that total choline and lactate/lipid levels were significantly higher in the metastasis-permissive environment. Prostate cancers are usually characterized by reduced or absent citrate polyamines and elevated total choline (7). The elevation of total choline has been shown to be a significant predictor of the pathologic Gleason score (7). Higher lactate levels have been observed in human prostate cancer biopsies compared to healthy glandular and stromal tissues (37). High local levels of lactate have been previously associated with a high risk of incidence of metastasis in head and neck and cervical cancers (38,39).

Tumor pHe can influence a number of processes relevant to tumorigenesis and therapy. The intracellular pH (pHi) in tumor cells is usually normal or slightly alkaline, but pHe is usually acid compared with normal tissue (40). In this study, we confirmed that pHe was acidic in both environments. However, orthotopic tumors were more acidic, despite a higher vascular volume. The more acidic pHe observed in the orthotopic tumors is consistent with the higher lactate/lipid signal observed in these tumors. The higher proliferation rate, as detected by the significant increase in mitotic figures in orthotopic tumors may have contributed to its more acidic pHe.

Previous studies have shown that an acidic pHe is associated with metastasis (41). Low pHe selects for phenotypes that are more invasive, as shown for melanoma cells (42). Additionally, Rofstad *et al.*, have observed that acidic pHe promoted experimental pulmonary metastasis of human melanoma cells by up-regulating the expression of the proteolytic enzymes MMP-2, MMP-9, cathepsin B, and cathepsin L and the pro-angiogenic factors VEGF-A and IL-8 (41). Acidic pHe has also been found to induce interleukin-8 (IL-8) expression, a cytokine that induces angiogenesis, vascular permeability, and has been associated with the metastatic potential of human prostate cancer cells (43,44). Increasing tumor pHe with oral bicarbonate therapy significantly reduced the incidence of metastases in experimental models of breast and prostate cancer without affecting the systemic pH and the growth rate of the primary tumors (8).

Despite the higher vascular volume in the orthotopic site, hypoxic regions between orthotopic and heterotopic tumors were comparable. The higher proliferation rate, and the associated increase of oxygen consumption, may explain the lack of difference in regions of hypoxia between the two sites. Interestingly, we observed hypoxic cancer cells in lymph node metastasis and ascites fluid from orthotopically implanted prostate tumors. Hypoxia has been previously observed in lymph node metastases of breast cancer patients (45). Increased microvascular

permeability of tumor vasculature is one of the causes of malignant ascites formation; increased VEGF levels are observed in malignant ascites that further promote the build-up of protein-containing fluid (46). The obstruction of lymphatic vessels by tumor invasion is also thought to significantly contribute to malignant ascites (46). Cells released into the peritoneal cavity no longer have a vascular supply of oxygen and nutrients (47), which may explain the expression of EGFP observed in the cancer cells detected in ascites fluid. Yang *et al.*, have shown that ovarian and gastric tumor cells gained some degree of protection from oxidative and free radical derived damage in ascites (47). Since hypoxic cancer cells are resistant to radiation and chemotherapy (48,49), the presence of hypoxic cancer cells in ascites fluid and lymph nodes, may further contribute to poor treatment outcome in metastatic disease.

Collectively these data suggest a profound influence of the tumor microenvironment on metastasis and the feasibility of identifying noninvasive clinically translatable parameters of metastasis-permissive environments. These parameters can also be used to monitor therapies targeting these environments to prevent or inhibit metastasis.

It is possible that the renal capsule or other organs may provide an environment that is as permissive as the prostate for metastasis to occur, compared to the subcutaneous site. Our purpose in these studies was to characterize a metastasis-permissive environment compared to a non-permissive environment. Since we were studying prostate cancer cells we chose the prostate for implantation, but it will be informative to compare the parameters and cell line studied here in metastasis-permissive implantation sites other than the prostate, as well as in non-permissive environments, to further validate the consistency of these characteristics.

The studies described here were performed with tumor growth in two very different sites. Clinically, prostate cancer typically arises in the glandular cells but the relationship between the location of tumor growth in the prostate and the formation of metastasis is not clear. Cancer cells to some extent establish their own microenvironment. This microenvironment is dictated by the genetic make-up of the cells, and as shown here, by the environment that the cells grow in. Future translational studies determining the ability of these parameters to predict subsequent formation of metastasis from prostate cancer are necessary to further validate these observations.

Acknowledgments

Abbreviations footnote

Cho	free intracellular choline
GPC	glycerophosphocholine
EGFP	enhanced green fluorescent protein
HIF	hypoxia-inducible factor
HRE	hypoxia response element
MR	magnetic resonance
MRS	magnetic resonance spectroscopy
MRSI	magnetic resonance spectroscopic imaging

MVD	microvessel density
PC	phosphocholine
pHe	extracellular
pH PSP	permeability-surface-area-product
tCho	total choline-containing metabolites (GPC+PC+Cho)

References

1. Greenlee RT, Hill-Harmon MB, Murray T, Thun M. Cancer statistics. CA Cancer J Clin 2001;51(1): 15–36. [PubMed: 11577478]

2. Taylor BS, Varambally S, Chinnaiyan AM. Differential proteomic alterations between localised and metastatic prostate cancer. Br J Cancer 2006;95(4):425–30. [PubMed: 16880794]

3. Hanahan D, Weinberg RA. The hallmarks of cancer. Cell 2000;100(1):57–70. [PubMed: 10647931]

4. Weidner N, Carroll PR, Flax J, Blumenfeld W, Folkman J. Tumor angiogenesis correlates with metastasis in invasive prostate carcinoma. Am J Pathol 1993;143(2):401–9. [PubMed: 7688183]

5. Liao D, Johnson RS. Hypoxia: a key regulator of angiogenesis in cancer. Cancer Metastasis Rev 2007;26(2):281–90. [PubMed: 17603752]

6. Zhang H, Gao P, Fukuda R, et al. HIF-1 inhibits mitochondrial biogenesis and cellular respiration in VHL-deficient renal cell carcinoma by repression of C-MYC activity. Cancer Cell 2007;11(5):407–20. [PubMed: 17482131]

7. Kurhanewicz J, Swanson MG, Nelson SJ, Vigneron DB. Combined magnetic resonance imaging and spectroscopic imaging approach to molecular imaging of prostate cancer. J Magn Reson Imaging 2002;16(4):451–63. [PubMed: 12353259]

8. Robey IF, Baggett BK, Kirkpatrick ND, et al. Bicarbonate Increases Tumor pH and Inhibits Spontaneous Metastases. Cancer Res. 2009

9. Miller FR. Comparison of metastasis of mammary tumors growing in the mammary fatpad versus the subcutis. Invasion Metastasis 1981;1(4):220–6. [PubMed: 7188387]

10. Waters DJ, Janovitz EB, Chan TC. Spontaneous metastasis of PC-3 cells in athymic mice after implantation in orthotopic or ectopic microenvironments. Prostate 1995;26(5):227–34. [PubMed: 7753708]

11. Havens AM, Pedersen EA, Shiozawa Y, et al. An in vivo mouse model for human prostate cancer metastasis. Neoplasia 2008;10(4):371–80. [PubMed: 18392141]

12. An Z, Wang X, Geller J, Moossa AR, Hoffman RM. Surgical orthotopic implantation allows high lung and lymph node metastatic expression of human prostate carcinoma cell line PC-3 in nude mice. Prostate 1998;34(3):169–74. [PubMed: 9492844]

13. Thomlinson RH, Gray LH. The histological structure of some human lung cancers and the possible implications for radiotherapy. Br J Cancer 1955;9(4):539–49. [PubMed: 13304213]

14. Lu CW, Lin SC, Chen KF, Lai YY, Tsai SJ. Induction of pyruvate dehydrogenase kinase-3 by hypoxia-inducible factor-1 promotes metabolic switch and drug resistance. J Biol Chem 2008;283(42):28106–14. [PubMed: 18718909]

15. Semenza GL. Regulation of cancer cell metabolism by hypoxia-inducible factor 1. Semin Cancer Biol 2009;19(1):12–6. [PubMed: 19114105]

16. Raman V, Artemov D, Pathak AP, et al. Characterizing vascular parameters in hypoxic regions: a combined magnetic resonance and optical imaging study of a human prostate cancer model. Cancer Res 2006;66(20):9929–36. [PubMed: 17047055]

17. Bhujwalla ZM, Artemov D, Natarajan K, Solaiyappan M, Kollars P, Kristjansen PE. Reduction of vascular and permeable regions in solid tumors detected by macromolecular contrast magnetic resonance imaging after treatment with antiangiogenic agent TNP-470. Clin Cancer Res 2003;9(1): 355–62. [PubMed: 12538488]

18. Ogan MD. Albumin labeled with Gd-DTPA: an intravascular contrast-enhancing agent for magnetic resonance blood pool imaging: preparation and characterization. Invest Radiol 1988;23(12):961. [PubMed: 3204001]

19. Bhujwalla ZM, Artemov D, Natarajan K, Ackerstaff E, Solaiyappan M. Vascular differences detected by MRI for metastatic versus nonmetastatic breast and prostate cancer xenografts. Neoplasia 2001;3 (2):143–53. [PubMed: 11420750]

20. Tkac I, Starcuk Z, Choi IY, Gruetter R. In vivo 1H NMR spectroscopy of rat brain at 1 ms echo time. Magn Reson Med 1999;41(4):649–56. [PubMed: 10332839]

21. Bolan PJ, Meisamy S, Baker EH, et al. In vivo quantification of choline compounds in the breast with 1H MR spectroscopy. Magn Reson Med 2003;50(6):1134–43. [PubMed: 14648561]

22. van Sluis R, Bhujwalla ZM, Raghunand N, et al. In vivo imaging of extracellular pH using 1H MRSI. Magn Reson Med 1999;41(4):743–50. [PubMed: 10332850]

23. Paget S. The distribution of secondary growths in cancer of the breast. The Lancet 1889;133:571–3.

24. Burton JB, Priceman SJ, Sung JL, et al. Suppression of prostate cancer nodal and systemic metastasis by blockade of the lymphangiogenic axis. Cancer Res 2008;68(19):7828–37. [PubMed: 18829538]

25. Chen B, Pogue BW, Zhou X, et al. Effect of tumor host microenvironment on photodynamic therapy in a rat prostate tumor model. Clin Cancer Res 2005;11(2 Pt 1):720–7. [PubMed: 15701861]

26. Singh RK, Bucana CD, Gutman M, Fan D, Wilson MR, Fidler IJ. Organ site-dependent expression of basic fibroblast growth factor in human renal cell carcinoma cells. Am J Pathol 1994;145(2):365–74. [PubMed: 8053494]

27. Zechmann CM, Woenne EC, Brix G, et al. Impact of stroma on the growth, microcirculation, and metabolism of experimental prostate tumors. Neoplasia 2007;9(1):57–67. [PubMed: 17325744]

28. Weidner N, Semple JP, Welch WR, Folkman J. Tumor angiogenesis and metastasis--correlation in invasive breast carcinoma. N Engl J Med 1991;324(1):1–8. [PubMed: 1701519]

29. Takagi K, Takada T, Amano H. A high peripheral microvessel density count correlates with a poor prognosis in pancreatic cancer. J Gastroenterol 2005;40(4):402–8. [PubMed: 15870976]

30. Loges S, Clausen H, Reichelt U, et al. Determination of microvessel density by quantitative real-time PCR in esophageal cancer: correlation with histologic methods, angiogenic growth factor expression, and lymph node metastasis. Clin Cancer Res 2007;13(1):76–80. [PubMed: 17200341]

31. Paez-Ribes M, Allen E, Hudock J, et al. Antiangiogenic therapy elicits malignant progression of tumors to increased local invasion and distant metastasis. Cancer Cell 2009;15(3):220–31. [PubMed: 19249680]

32. Cai KX, Tse LY, Leung C, Tam PK, Xu R, Sham MH. Suppression of lung tumor growth and metastasis in mice by adeno-associated virus-mediated expression of vasostatin. Clin Cancer Res 2008;14(3):939–49. [PubMed: 18245558]

33. Huang SF, Kim SJ, Lee AT, et al. Inhibition of growth and metastasis of orthotopic human prostate cancer in athymic mice by combination therapy with pegylated interferon-alpha-2b and docetaxel. Cancer Res 2002;62(20):5720–6. [PubMed: 12384530]

34. Dong Z, Greene G, Pettaway C, et al. Suppression of angiogenesis, tumorigenicity, and metastasis by human prostate cancer cells engineered to produce interferon-beta. Cancer Res 1999;59(4):872–9. [PubMed: 10029078]

35. Abramovitch R, Itzik A, Harel H, Nagler A, Vlodavsky I, Siegal T. Halofuginone inhibits angiogenesis and growth in implanted metastatic rat brain tumor model--an MRI study. Neoplasia 2004;6(5):480–9. [PubMed: 15548356]

36. Tuomela JM, Valta MP, Vaananen K, Harkonen PL. Alendronate decreases orthotopic PC-3 prostate tumor growth and metastasis to prostate-draining lymph nodes in nude mice. BMC Cancer 2008;8:81. [PubMed: 18371232]

37. Swanson MG, Zektzer AS, Tabatabai ZL, et al. Quantitative analysis of prostate metabolites using 1H HR-MAS spectroscopy. Magn Reson Med 2006;55(6):1257–64. [PubMed: 16685733]

38. Walenta S, Salameh A, Lyng H, et al. Correlation of high lactate levels in head and neck tumors with incidence of metastasis. Am J Pathol 1997;150(2):409–15. [PubMed: 9033256]

39. Walenta S, Wetterling M, Lehrke M, et al. High lactate levels predict likelihood of metastases, tumor recurrence, and restricted patient survival in human cervical cancers. Cancer Res 2000;60(4):916–21. [PubMed: 10706105]

40. Garcia-Martin ML, Herigault G, Remy C, et al. Mapping extracellular pH in rat brain gliomas in vivo by 1H magnetic resonance spectroscopic imaging: comparison with maps of metabolites. Cancer Res 2001;61(17):6524–31. [PubMed: 11522650]

41. Rofstad EK, Mathiesen B, Kindem K, Galappathi K. Acidic extracellular pH promotes experimental metastasis of human melanoma cells in athymic nude mice. Cancer Res 2006;66(13):6699–707. [PubMed: 16818644]

42. Moellering RE, Black KC, Krishnamurty C, et al. Acid treatment of melanoma cells selects for invasive phenotypes. Clin Exp Metastasis 2008;25(4):411–25. [PubMed: 18301995]

43. Kitadai Y, Haruma K, Sumii K, et al. Expression of interleukin-8 correlates with vascularity in human gastric carcinomas. Am J Pathol 1998;152(1):93–100. [PubMed: 9422527]

44. Matsushima H, Goto T, Hosaka Y, Kitamura T, Kawabe K. Correlation between proliferation, apoptosis, and angiogenesis in prostate carcinoma and their relation to androgen ablation. Cancer 1999;85(8):1822–7. [PubMed: 10223578]

45. Van den Eynden GG, Van der Auwera I, Van Laere SJ, et al. Angiogenesis and hypoxia in lymph node metastases is predicted by the angiogenesis and hypoxia in the primary tumour in patients with breast cancer. Br J Cancer 2005;93(10):1128–36. [PubMed: 16251878]

46. Adam RA, Adam YG. Malignant ascites: past, present, and future. J Am Coll Surg 2004;198(6):999–1011. [PubMed: 15194082]

47. Yang W, Toffa SE, Lohn JW, Seifalian AM, Winslet MC. Malignant ascites increases the antioxidant ability of human ovarian (SKOV-3) and gastric adenocarcinoma (KATO-III) cells. Gynecol Oncol 2005;96(2):430–8. [PubMed: 15661232]

48. Marignol L, Coffey M, Lawler M, Hollywood D. Hypoxia in prostate cancer: a powerful shield against tumour destruction? Cancer Treat Rev 2008;34(4):313–27. [PubMed: 18334284]

49. Gillies RJ, Raghunand N, Karczmar GS, Bhujwalla ZM. MRI of the tumor microenvironment. J Magn Reson Imaging 2002;16(4):430–50. [PubMed: 12353258]
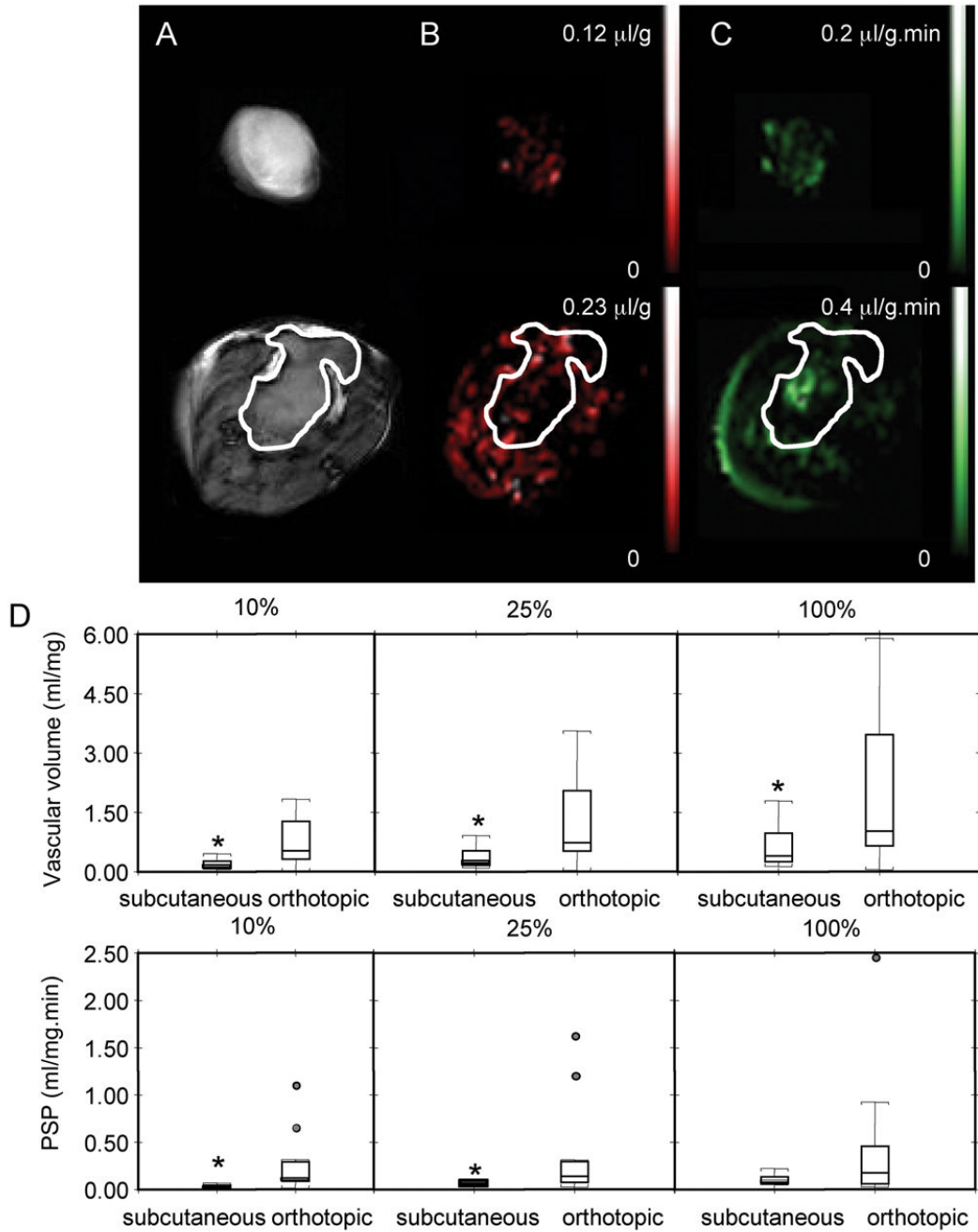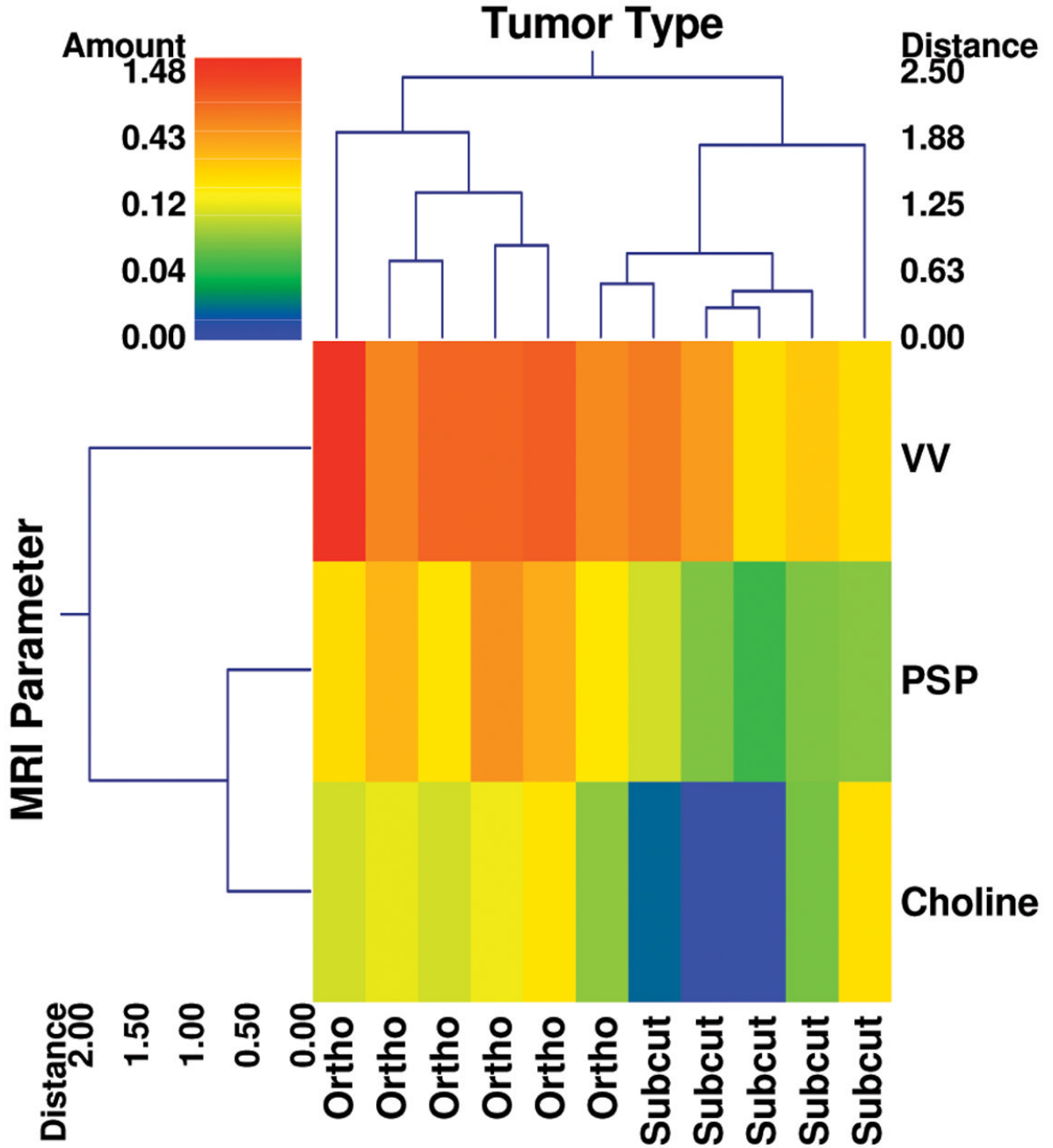
Figure 1.
Vascular analyses of subcutaneous (upper panel) and orthotopic (lower panel) tumors. (A) Diffusion-weighted images, (B) vascular volume maps, (C) PSP maps (scale bar = 5 mm) of a subcutaneous tumor (344 mm^3) and an orthotopic tumor (367 mm^3). Diffusion-weighted images were acquired with an in-plane spatial resolution of 250 μm, vascular volume maps and PSP maps were acquired with an in-plane spatial resolution of 125 or 250 μm respectively. (D) Box-and-whisker plots of total vascular volume and total PSP in subcutaneous (n=9) and orthotopic (n=12) tumors. The three plots represent analysis of the highest 10%, 25%, and all VV pixels (*$p \leq 0.05$).
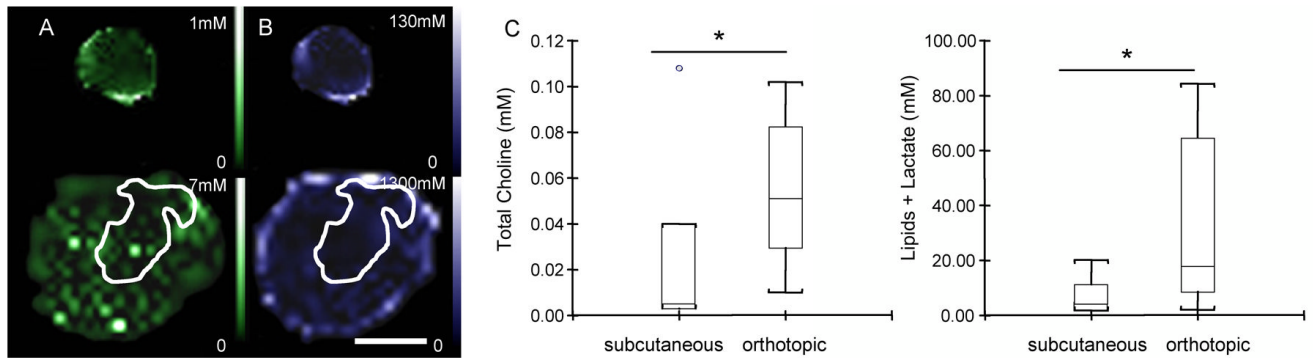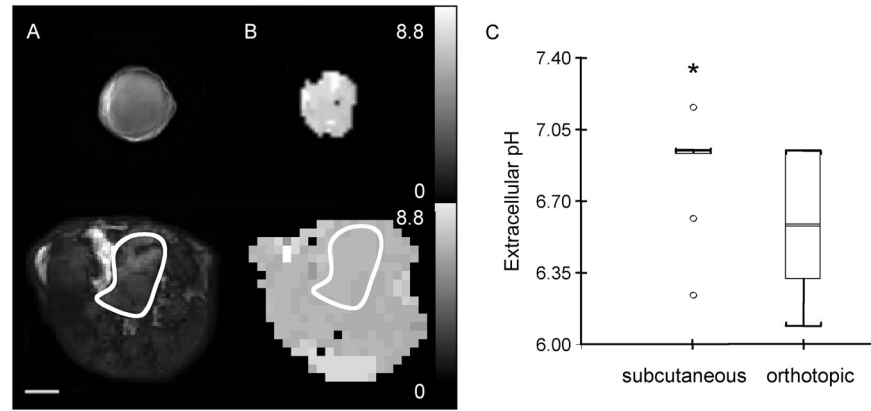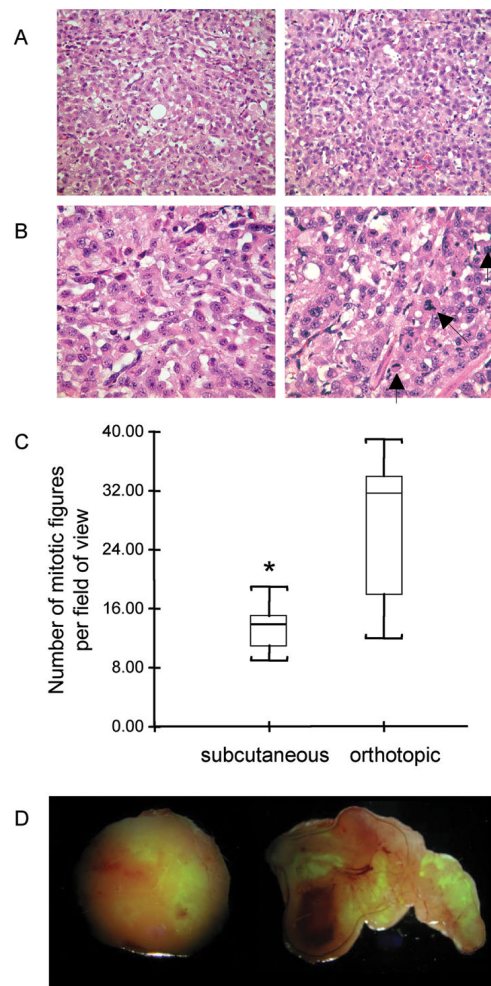
Figure 2.
Metabolic analyses of subcutaneous (upper panel) and orthotopic (lower panel) tumors. (A) total choline maps, (B) lactate/lipid maps (scale bar = 1 cm) of the subcutaneous (344 mm^3) and orthotopic (367 mm^3) tumor shown in Figure 1. Metabolite maps were acquired with a 1 × 1 mm in-plane resolution from a 4 mm slice. (C) Box-and-whisker plots of total choline and lipid/lactate concentrations in subcutaneous (n=7) and orthotopic (n=13) tumors (*$p \leq 0.05$).

Figure 3.
A double dendrogram illustrating the feasibility of clustering orthotopic and subcutaneous microenvironments on the basis of three imaging parameters measured *in vivo*: vascular volume (VV), permeability-surface-area-product (PSP) and total choline concentration. The color bar represents the range of the variables color coded according to a log scale to accommodate the entire dynamic range of each variable. VV, PSP and total choline data clustered into two distinct groups, with the orthotopic group exhibiting elevated values for each parameter (hotter colors) compared to the subcutaneous group. The distance axis on the dendrogram represents the distance or dissimilarity between the two clusters. Also, apparent from this "double" dendrogram is that the PSP and total choline cluster together for this group of animals.
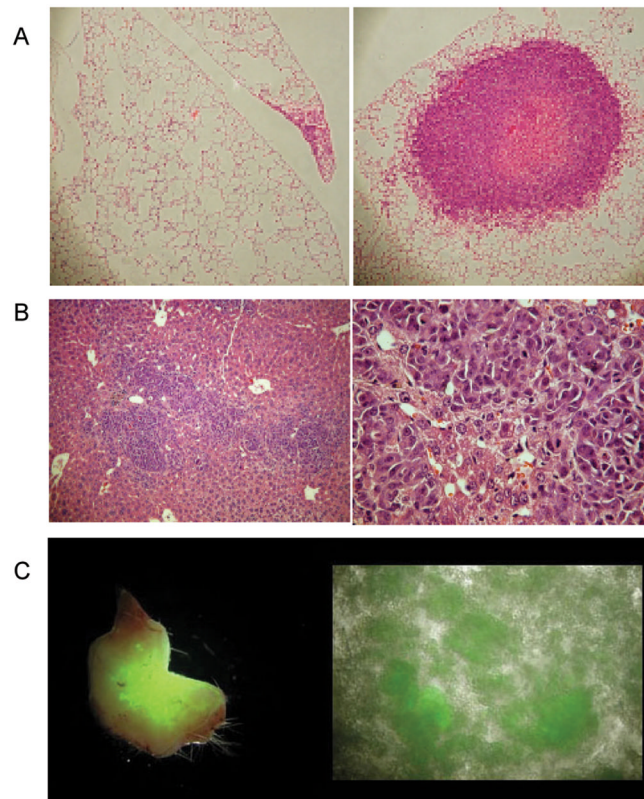
Figure 4.
pHe analyses of subcutaneous and orthotopic tumors. (A) Diffusion-weighted image and (B) pHe map of a subcutaneous tumor (260 mm^3) (upper panel) and of an orthotopic tumor (247 mm^3) (lower panel). pHe maps were acquired with a 1×1 mm^2 in-plane resolution from a 4 mm slice. Scale bar represents 5 mm. (C) Box-and-whisker plot of pHe values from subcutaneous (n=12) and orthotopic (n=10) tumors (*$p \leq 0.05$).

Figure 5.
Mitotic figures and EGFP expression in primary tumors. (A) Representative microscopy images of 5 μm thick H&E stained sections obtained at ×20 magnification from a subcutaneous (left) and an orthotopic (right) tumor. The corresponding images obtained at x40 magnification are shown in (B). Mitotic figures in the orthotopic tumor are marked by arrows. (C) Box-and-whisker plot of the quantification of mitotic figures from 20 fields of view of 7 different slides for both orthotopic and subcutaneous tumors (*$p \leq 0.05$). (D) EGFP expression maps overlaid with white light images of an excised subcutaneous (left) and orthotopic (right) tumor. Hypoxic fluorescing cells are evident in these images. Images were acquired at ×1 magnification.

Figure 6.
Metastatic dissemination and EGFP expression in metastases. (A) Representative microscopy images of 5 μm thick H&E stained sections obtained at ×10 magnification from the lungs of a mouse with a subcutaneous (left) and orthotopically (right) implanted tumor. (B) Representative microscopy images of a 5 μm thick H&E stained section from the liver of a mouse with an orthotopic tumor, obtained at ×10 magnification (left) and ×40 magnification (right). (C) EGFP expression in lymph node excised from an orthotopically implanted mouse (left), ascites fluid from an orthotopically implanted mouse (right). Hypoxic fluorescing cells are evident in these images. Images were acquired at ×1 magnification.